Experimental and numerical study of thermal and electrical potential of BIPV/T collector in the form of air-cooled photovoltaic roof tile

Jakub Lukasik , Jan Wajs [*]

Gdansk University of Technology, Faculty of Mechanical Engineering and Ship Technology, Institute of Energy, Narutowicza 11/12, 80-233 Gdansk, Poland

ARTICLE INFO

ABSTRACT

Among renewable energy sources, Building-Integrated Photovoltaic/Thermal (BIPV/T) systems are gaining increasing interest. To improve their economic competitiveness, technologies that increase their efficiency are searched for. The paper is devoted to evaluating the impact of various air-cooling configurations on the thermal and electrical performance of a photovoltaic roof tile. A numerical model of the own experimental system was developed in the ANSYS Fluent software for a wide range of input variables. The original approach based on the SST k-ω turbulence model, Discrete Ordinates radiation model, and the use of Solar Load module were proposed. Such a numerical model allows representation of semi-transparent layers and variable solar irradiance, which is a unique realization of real system modelling. Numerous analyses conducted indicate a higher heat recovery potential for an airflow duct with a height of 25 mm for all configurations analysed. The highest value of recovered heat flux was approximately 330 W/m^2 under conditions of a volumetric air flow rate of 7.5 m^3/h and solar irradiance equal to 900 W/m^2. Good agreement of the results of the multivariant CFD simulations with new experimental ones was confirmed. Insight into the flow phenomena behind the achieved thermal results supplemented the knowledge. The highest electrical efficiency obtained experimentally was 5.76 % for a channel with a height of 50 mm, volumetric flow rate equal to 7.5 m^3/h and solar irradiance equal to 600 W/m^2. The presented methodology and the results obtained can be useful in research devoted to optimising BIPV/T air-based cooling systems, which will then be tested in-situ. Moreover, new experimental data collection can be used for the verification of numerical models.

1. Introduction

For years, there have been many efforts taken to create low-emission economies functioning in accordance with the idea of sustainable development. The main concept is related to maximisation of the share of energy coming from renewable energy sources (RES) in the total mix of consumed energy. One of the fastest growing branches of renewable energy is solar energy, especially the photovoltaic (PV) sector [1]. Considering the growth rate of the new installed capacity, related to the potential of solar energy [2], it becomes reasonable to look for new ways to encourage entities to invest in a PV installations. Building-Integrated Photovoltaics (BIPV) and its development in a form of the Building-Integrated Photovoltaic/Thermal (BIPV/T) system, where in addition to producing electricity, heat energy is also recovered, is a solution that has become more and more popular in recent years.

The most common way to receive heat from BIPV/T collectors is an active cooling techniques using gaseous or liquid cooling medium [3].

Heat collection methods, proposed in the literature, are based on the use of phase change materials (PCM) [4], nanofluids [5], heat pipes [6], direct evaporation of the refrigerant, [7], thermoelectric cooling [8] or bifluidic systems [9]. Removing heat from the modules reduces the operating temperature of PV cells. This prevents a decrease in generated power, the value of which is determined by the temperature coefficient of PV module, defined in relation to a growth in the module operating temperature by 1 K. For the most popular monocrystalline and polycrystalline modules on the market, the power decrease ranges from 0.25 % to 0.5 % of the power determined at the maximum power point (MPP) for standard test conditions (STC) [10]. Therefore, lowering the operating temperature with constant solar irradiance causes an increase in the generation of electric power and increases the economic competitiveness of the photovoltaic installation. Furthermore, reducing the temperature can have a positive impact on the lifetime of the module, as well as limitation of its efficiency decrease over the years, its protection against overheating, degradation of the structure and loss of properties of the Ethylene-Vinyl Acetate (EVA) foil [11]. The issue of effective heat

---

Nomenclature

a	absorption coefficient [1/m]
A	active area of the module [m^2]
A_c	total area of the module wetted by the cooling medium [m^2]
A_f	cross-sectional area of the flow [m^2]
c	specific heat [J/(kg•K)]
D_h	hydraulic diameter of the air duct [m]
e	specific energy [J/kg]
$\vec{g}$	vector of gravity acceleration [m/s^2]
G	solar irradiance [W/m^2]
h	specific enthalpy [J/kg]
h_{nat}	convective heat transfer coefficient [W/(m^2•K)]
I	radiation intensity [W/m^2]
I_e	electrical current [A]
I_t	turbulence intensity [-]
k	turbulence kinetic energy [m^2/s^2]
k_{eff}	effective thermal conductivity coefficient [W/(m•K)]
m	number of variables in the function [-]
n	number of measurement points [-]
n_{ref}	refractive index [-]
p	pressure [Pa]
P_k	production term [kg/(m·s^3)]
P	generated power [W]
q	heat flux [W/m^2]
$\vec{r}$	position vector [m]
Re	Reynolds number [-]
s	path length [m]
$\vec{s}$	direction vector [-]
S	strain rate [s^{-1}]
$\vec{s'}$	scattering direction vector [-]
t	time [s]
T	temperature [K]
u_T	friction velocity at the closest wall [m/s]
U	voltage [V]
v	velocity magnitude [m/s]
$\vec{v}$	velocity vector [m/s]
$\dot{V}$	volumetric air flow rate [m^3/s]
x	variable
y	function describing a given quantity
y^+	dimensionless wall distance [-]
y_p	absolute distance from the wall [m]

Greek symbols

δ	relative difference [-]
$\Delta(x)$	measurement uncertainty of a device measuring the value of a variable x
η	efficiency [-]
μ	dynamic viscosity [kg/(m•s)]
μ_T	turbulent viscosity [kg/(m•s)]
ν	kinematic viscosity [m^2/s]
ρ	density [kg/m^3]
σ	Stefan-Boltzmann constant [W/(m^2•K^4)]
σ_m	standard deviation
σ_s	scattering coefficient [1/m]
$\overline{\overline{\tau}}$	shear stress tensor [Pa]
$\overline{\overline{\tau}}_{eff}$	effective stress tensor [Pa]
Φ	phase function [-]
ω	specific dissipation rate [s^{-1}]
Ω	solid angle [sr]

Indexes

air	related to the air
amb	related to the ambient conditions
avg	averaged value
CFD	coming from CFD calculations
ex	coming from experimental measurements
i	measured point number
in	related to the inlet
j	variable number
MPP	related to the maximum power point
out	related to the outlet
PV	related to the PV roof tile
surf	related to the front surface of the module
th	thermal
tot	total value

Abbreviations

BIPV	Building-Integrated Photovoltaic
BIPV/T	Building-Integrated Photovoltaic/Thermal
CFD	Computational Fluid Dynamics
DO	Discrete Ordinates
EVA	Ethylene-Vinyl Acetate
FVM	Finite Volume Method
LRNM	Low Reynolds Number Modelling
MPP	Maximum Power Point
nZEB	nearly Zero Energy Building
RES	Renewable Energy Sources
PCM	Phase Change Material
PV	Photovoltaic
PVF	Polyvinyl Fluoride
PV/T	Photovoltaic/Thermal
RANS	Reynolds-Averaged Navier-Stokes
RTE	Radiative Transfer Equation
SST	Shear Stress Transport
STC	Standard Test Conditions

removal from PV modules becomes even more important in the case of BIPV and BIPV/T systems, due to the integration of the modules with the building structure and their exposure to high temperature [12]. This is due to the limited ability of the surrounding air to remove heat, resulting from the specific location of the module, dictated by technical and aesthetic aspects.

1.1. Air cooling state-of-the-art

Various techniques of heat collection from PV modules, solar thermal collectors, and photovoltaic/thermal (PV/T) collectors were reported in the literature. The use of air as a heat transport medium is considered one of the most promising ways to remove heat from BIPV/T collectors [12]. Air cooling has a number of advantages over alternative solutions, such as unlimited availability, no acquisition costs, no negative environmental impact, simplicity of construction, low cost, no problems with boiling, freezing, leaking, and increased risk of moisture in electrical components [13]. The biggest disadvantage of air cooling, compared to competitive liquid-based systems, is the unfavourable thermophysical properties of air, such as low thermal conductivity, low heat capacity, and low values of the heat transfer coefficient for air cooling. This has a negative impact on the efficiency of heat removal. Thus, standard air cooling systems usually possess lower overall efficiency than their liquid counterparts [14]. In response to these

shortages, effective methods of heat transfer intensification dedicated to PV/T and BIPV/T systems are constantly being searched for, and in the literature a number of them were proposed. These include the use of additional glazing and double-pass configurations [15,16], the use of systems with multiple inlets [17], increasing the roughness of the heat exchange surface and flow turbulisation by V-shaped ribs [18], winglets and grooves [19], various rib roughness arrangements [20,21], corrugation [22], development of heat exchange surfaces [23,24], or the use of the jet impingement technique [25].

In the case of PV/T or BIPV/T systems, great importance is placed on the effective recovery of low-temperature waste heat. It is considered to be used for preheating fresh air in ventilation units [26], in a farm buildings to heat granaries, stables, hen houses or rabbit houses [27] as well as for industrial applications [28].

Focussing on photovoltaic roof tile, it is necessary to narrow the issue of PV/T and BIPV/T collectors air cooling to a systems with air flowing through a duct located under the absorber. Succeeding are examples of the research conducted on such arrangement of cooling channels.

Xie et al. [29] numerically and experimentally evaluated an air-cooled PV/T collector with a double serpentine runner. The studies concentrated on the influence of various parameters on the achieved electrical and thermal-hydraulic performance. The following parameters were considered: the number of side partitions (4–18), the height of the partitions (35–145 mm), the length of the central partitions (500–900 mm), and the air mass flow rate (0.01–0.05 kg/s). The proposed collector was characterised by thermal, electrical, total, and exergy efficiency in the ranges $31.2-42.3$ %, $11.3-12.5$ %; $47.3-51.1$ % and $9.8-11.8$ % respectively.

Hussien et al. [30], experimentally and numerically tested two configurations of PV modules cooling, differing in the way of air supply. In the first configuration, the blower forced air through a wooden flow channel, and in the second, the flow was forced by 8 small fans symmetrically placed at the back of the module. A blower cooling reduced the average temperature of the module surface by 5.4 K, increased module efficiency by 1.34 % and allows for energy savings of 4.2 %. The numerical tests showed high agreement with the experimental results in the thermal aspect.

Arslan et al. [14] performed computational fluid dynamics (CFD) simulations of an air-cooled PV/T collector with a proposed copper fins placed in the flow channel. The tests were performed for two values of mass flow rate (0.03109 and 0.04553 kg/s) and compared with their own experimental data. The average thermal and electrical efficiency at a lower flow rate was 37.10 % and 13.56 %, respectively, while at its higher value it was 49.5 % and 13.98 %. Very good agreement was obtained between the numerical and experimental results. The authors also emphasised small differences between the experimentally obtained value of the average air temperature at the air duct outlet and the values obtained numerically with different turbulence models.

Kasaeian et al. [31] conducted experiments on the effects of the air mass flow rate (from 0.018 to 0.154 kg/s) and the height of the flow channel (50, 100 and 150 mm) on electrical and thermal performance of the photovoltaic system. The results obtained indicated that reduction of channel height increases the thermal efficiency, but does not have a significant impact on the electrical efficiency. In each case, the overall efficiency increases with an increase in air flow rate.

Patil et al. [32] performed an experimental analysis of an air cooling system with a wooden flow channel. Attention was focused on examining the effectiveness of the proposed cooling system in terms of reducing the operating temperature of the PV module. The tests were carried out at mass flow rates in the range of 0.04–0.08 kg/s. At the highest mass flow rate, the average module temperature decreased by 9 K. The maximum electrical efficiency of the module increased from 7 % to 12.6 %, compared to the configuration without cooling.

In the research conducted by Dunne et al. [33], attention was focused on assessing the impact of the flow channel height and the velocity of cooling air on the thermal and electrical performance obtained from the

PV module and PV/T collector. The proposed air duct with a height of 50 mm enabled the improvement of the electrical efficiency of the PV module by 13.67 %. The temperature of the PV module was reduced from 77.9 °C to 53.4 °C. On the basis of parametric tests, it was found that an increasing duct depth negatively affects the electrical and thermal efficiency. The overall efficiency of the system increases with an increase in the air velocity in the duct.

1.2. Motivation and contribution to work

The literature overview exhibits that the most often are presented the results of tests carried out for classic PV modules or PV/T collectors, for a small number of configurations of input variables. Some of them refer only to the possibility of reducing the operating temperature of the PV module and increasing the generated power. The presented work contributes to the state of the art with the results of own work on the impact of selected operating conditions and cooling configuration of a PV roof tile on its electrical and thermal parameters. A wide range of solar irradiance (from 300 to 900 W/m^2) and volumetric air flow rates (from 0 to 7.5 m^3/h), covering a total of 46 different variants, were considered. Solar irradiance values cover the typical latitude range between 49° and 54° (Poland is among the countries located in this range), where the temporary values during the day range from 100 to 1000 W/m^2 [34]. The tested volumetric air flow rate values are an extension of previous studies presented by the authors [35,36]. Most of the literature focuses on studying higher air flow rate values, which may not be feasible in some applications. As an example of such application can be given an integration of the BIPV/T with an air source heat pump, where the air flow through the evaporator is provided by a fan operating with modulated power, adjusted to the temporary heat load of the facility.

The motivation of the authors to carry out this research is a lack of work on air cooling of BIPV/T systems, highlighted in the latest publications [12,33], which is particularly important in the face of the expected dynamic development of this sector. BIPV/T systems, as installations with high polygeneration potential, are perceived as one of the leading technologies that can help meet the requirements for nearly Zero Energy Buildings (nZEB) [37].

According to the identified literature gap, an analysis of photovoltaic roof tiles with air cooling was conducted. A multivariant comparison of the own results from an experimental tests and CFD simulations was done. Particular attention was paid to the thermal aspect and the potential for heat recovery. A dedicated numerical model, mapping the experimental stand and the operating conditions, was prepared in the ANSYS Fluent software. An original approach was proposed using the Discrete Ordinates (DO) radiation model, with the Solar Load module implemented. This allows for a good reflection of actual environmental conditions. The prepared model can be used as a useful tool in analysis of the impact of selected input variables on thermal-hydraulic as well as electrical efficiency indicators. The results may also provide a better understanding of the impact of flow channel geometry and cooling conditions on module performance, which may help in the design of more efficient and economic BIPV/T systems.

2. Metodology

2.1. Experimental setup

Experimental studies were carried out at the Institute of Energy of Gdansk University of Technology. The object of the research was the SolteQ Quad35 photovoltaic roof tile with cells made of monocrystalline silicon. The experimental stand is an extension of the system used by the authors in previous studies. Therefore, this section only briefly presents the experimental setup used and highlights the most important modifications. A detailed description of the research site can be found in [35]. Table 1 shows the technical specifications of the tested PV roof tile.

The tile was attached to a wooden casing acting as an air flow duct, in

Table 1
Technical specification of the SolteQ Quad35 photovoltaic roof tile.

Parameter	Value
Module dimensions	540 × 540 mm
Total / active area of the module	0.2916 / 0.2190 m^2
Dimensions of the single cell	156 × 156 mm
Operating temperature	−40 to +80 °C
Nominal power under STC	35 W ± 3 %
Operating voltage under STC	4.5 V
Operating current under STC	7.8 A
Unloaded voltage	4.9 V
Short-circuit current	8.2 A
Temperature coefficient of PV module	−0.5 ± 0.05 %/K

which baffles were installed to direct the flow of the medium. Ducts with a height of 25 mm (the value associated with the smallest thickness of battens and counterbattens found in housing construction) and 50 mm (resulting from the method of mounting PV roof tiles on metal hooks proposed by the manufacturer) were selected for the analysis. The structure of the casing and air flow duct is shown in Fig. 1.

The tile was illuminated by 20 halogen lamps with filaments of nominal power of 500 W, which acted as a sunlight simulator. The measurement of the solar irradiance falling on the module was carried out using the Kipp&Zonen CM6B pyranometer, the signal from which was led to the Meratronik Type V534 multirange voltmeter. The pyranometer was mounted in the upper part of the casing to not disturb the rays that fall on the PV roof tile. Due to the change in the position of the pyranometer relative to the centre of the module and the expected non-uniformity of the solar irradiance distribution on the surface of the tile, the actual solar irradiance distribution at nine reference points located in the geometrical centres of each cell was examined. For all tested reference values of solar irradiance, their actual values were determined at each point. The results obtained are presented in Fig. 2.

The average of 9 points, actual solar irradiance values, and their reference values as well as standard deviation, are presented in Table 2. The standard deviation of the measured values was calculated according to the following formula:
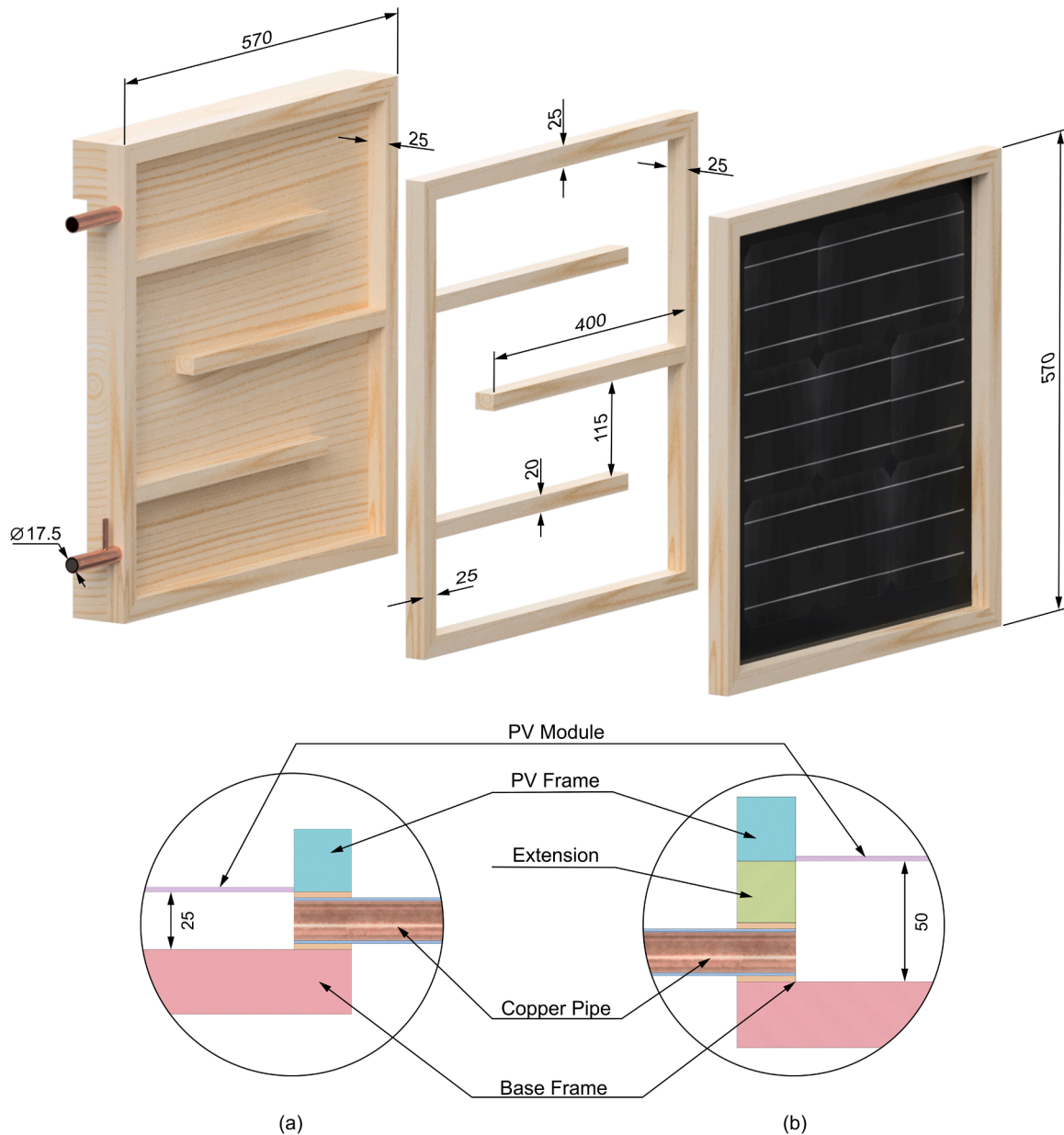

Fig. 1. The casing of the tested photovoltaic roof tile and cross-sections of the air ducts with a height of: (a) 25 mm and (b) 50 mm.
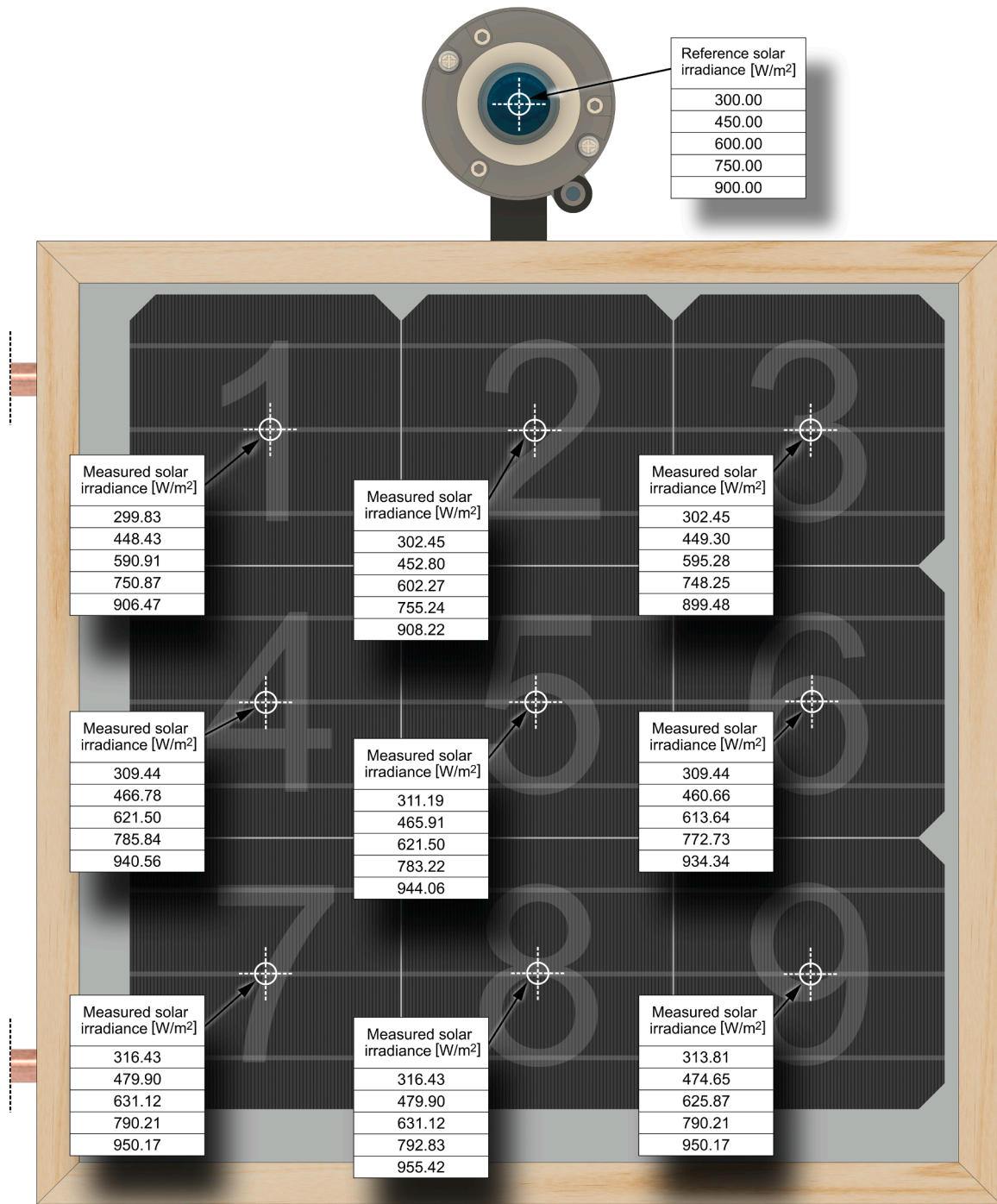
Fig. 2. Actual solar irradiance obtained at 9 measurement points.

Table 2
Reference and average solar irradiance at the front surface of the PV roof tile.

Reference solar irradiance [W/m^2]	Averaged actual solar irradiance [W/m^2]	Standard deviation [W/m^2]
300	309.05	5.86
450	464.26	11.67
600	614.80	14.36
750	774.38	17.18
900	932.11	20.30

$$\sigma_m = \sqrt{\frac{\sum_{i=1}^{i=9}\left(G_i - G_{avg}\right)^2}{n-1}} \tag{1}$$

where: n – number of measurement points; i – measuring point number; G_i – solar irradiance value at point i [W/m^2]; G_{avg}– average solar irradiance [W/m^2].

Table 3 lists the devices included in the data acquisition system along with their measurement uncertainties. Fig. 3 shows photos of the actual experimental stand with marked measuring devices.

Table 3
Measurement devices included in the data acquisition system.

Parameter	Device	Uncertainty
Solar irradiance	Kipp & Zonen CM6B + Meratronik Type V534	±40 W/m^2
Temperature on the surface of the module	Fluke 62 Mini	±1.5 °C
Temperature of the outer walls of the casing		
Voltage at the receiver	Vorel 81,780	±0.1 V
Current flowing through the load	Emos EM391	±0.2 A
Volumetric air flow rate	ROL 16	±0.1 m^3/h
Inlet/outlet air temperature	Type T thermocouples + Cropico 3001	±0.1 °C
Inlet/outlet stub pipes temperature		
Air temperature in the vicinity of the front surface of the module		

2.2. Mathematical formulation

One of the objectives of the investigation was to determine the energy benefits resulting from the cooling of the photovoltaic roof tile in the assumed range of the input variables tested. The average temperature of the module was determined from the formula:

$$T_{surf\_avg} = \frac{\sum_{i=1}^{i=9} T_{surf\_i}}{n} \tag{2}$$

where: T_{surf_i} – front face temperature of the module at point i [K].

The power generated in MPP was calculated as:

$$P_{MPP} = U_{MPP} \cdot I_{e\_MPP} \tag{3}$$

where: U_{MPP} – voltage at MPP [V]; I_{e_MPP} – electrical current at the MPP [A].

The electrical efficiency of the module was defined as:

$$\eta_{MPP} = \frac{P_{MPP}}{G \cdot A} \tag{4}$$

where: G – solar irradiance [W/m^2]; A – active area of the module [m^2].

The recovered heat flux was determined from the following formula:

$$q = \frac{\rho_{air\_avg} \cdot \dot{V} \cdot c_{avg} \cdot (T_{out} - T_{in})}{A_c} \tag{5}$$

where: ρ_{air_avg} – air density for average temperature between T_{in} and T_{out} [kg/m^3]; $\dot{V}$ – volumetric flow rate of air [m^3/s]; c_{avg}– average specific heat over a range of temperature values from T_{in} to T_{out} [J/(kg•K)]; T_{out} – temperature of the outlet air [K]; T_{in} – temperature of the inlet air [K]; A_c – total area of the module wetted by the cooling medium [m^2].

The CoolProp library of thermodynamic media was used to deter-mine the average density and average specific heat of the air. The thermal efficiency was related to the value of solar irradiance incident on the module and was determined as follows:

$$\eta_{th} = \frac{q}{G} \tag{6}$$

Overall efficiency was defined as the sum of electrical and thermal efficiency:

$$\eta_{tot} = \eta_{MPP} + \eta_{th} \tag{7}$$

To deal with numerous data, an own calculation script was con-structed in Microsoft Excel.

2.3. Numerical model

One of the key aspects was the development of a numerical thermal-flow model. CFD analysis was performed in Ansys Fluent 2021 R1 software. The geometry prepared in SpaceClaim mirrored the experi-mental one. The prepared physical model with marked boundary con-ditions is presented in Fig. 4.

The conformal tetragonal mesh was created, consisting of approxi-mately 949,000 cells for the geometry with a channel height of 25 mm and 1168,000 cells for 50 mm. To maintain satisfactory values of mesh quality, the mesh size was locally refined. Skewness at the level of 0.25 (average) for 25 mm and 0.24 (average) for 50 mm was obtained. In the fluid-solid contact zone, boundary layers were indicated using a fixed growth rate of 1.2. Sensitivity studies of a solution in relation to the number of mesh elements were performed. Meshes were tested in the range of up to 3020,000 cells for channel height of 25 mm and 3233,200 cells for channel height of 50 mm. The tests show that the use of finer mesh does not significantly increase the accuracy of the calculations of the considered parameters. Thus, the prepared mesh was chosen as sufficient in terms of the compromise between accuracy and calculation time. Fig. 5 shows an ultimately generated mesh for a system with a duct
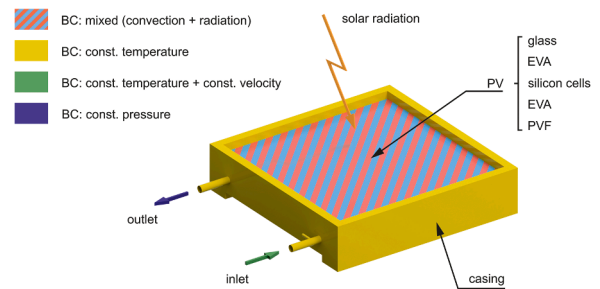

Fig. 4. Physical model of PV roof tile prepared for CFD analysis.
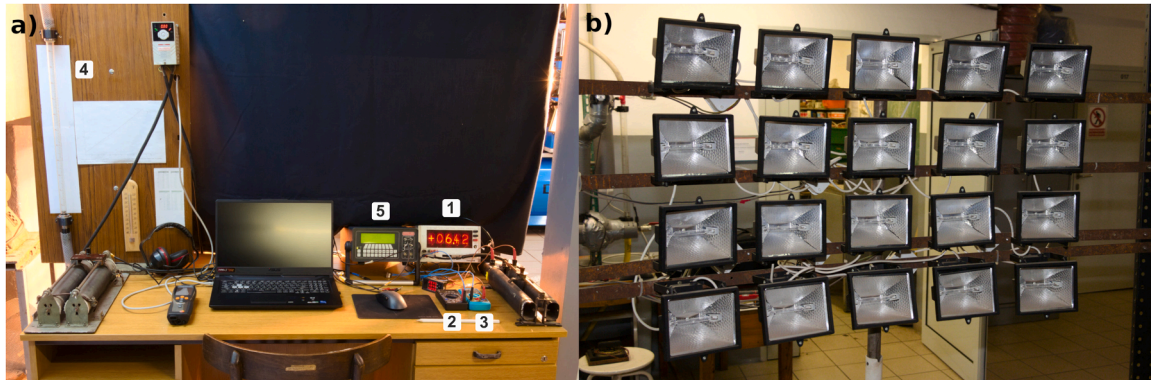

Fig. 3. (a) Measurement apparatus with data acquisition system: 1 – Meratronik Type V534, 2 – Vorel 81,780, 3 – Emos EM391, 4 – ROL 16, 5 – Cropico 3001; (b) solar radiation simulator.
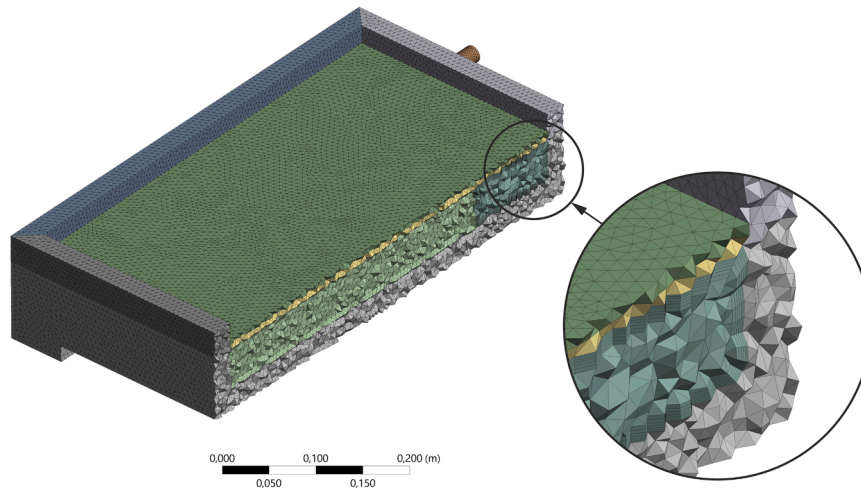
Fig. 5. Mesh for a system with an air duct of 50 mm height.

height of 50 mm.

Constant values of the thermophysical properties of the solid materials used were assumed. Their variability in the temperature range is small, so this simplified approach is most common in the literature [38, 39]. In the case of air, as in [33], a constant value of thermophysical properties was assumed due to the small impact of their variability on the results obtained in the tests. The exception is the air density, which was calculated using the Boussinesq approximation, with a given thermal expansion coefficient of 0.0034 K^{-1} [40]. All properties of the material are listed in Table 4. In the case of materials of the PV module, their thickness is given in brackets.

The finite volume method (FVM) was used to solve the thermal flow model, based on the differential equations of conservation of continuity, momentum, and energy. Simulations were conducted in a gravitational field as a steady state for a Newtonian fluid, with 3D geometry, without external mass and energy sources. Taking into account these assumptions, the equations took the form [43,44,45]:

Continuity equation:

$$\nabla\cdot\overrightarrow{v} = 0 \qquad (8)$$

where: ρ – fluid density [kg/m^3]; $\overrightarrow{v}$ – velocity vector [m/s].

Momentum conservation equation:

$$\nabla\cdot(\rho\,\overrightarrow{v}\,\overrightarrow{v}) = -\nabla p + \nabla\cdot\overline{\overline{\tau}} + \rho\,\overrightarrow{g} \qquad (9)$$

where: p – pressure [Pa]; $\overline{\overline{\tau}}$ – shear stress tensor [Pa]; $\overrightarrow{g}$ – vector of gravity acceleration [m/s^2].

Energy conservation equation:

$$\nabla\cdot(\overrightarrow{v}(\rho e + p)) = \nabla\cdot\left(k_{eff}\nabla T + \overline{\overline{\tau}}_{eff}\cdot\overrightarrow{v}\right) \qquad (10)$$

where: e – specific energy [J/kg]; k_{eff} – effective thermal conductivity coefficient including molecular and turbulent conductivity [W/(m•K)];

T – local temperature [K]; $\overline{\overline{\tau}}_{eff}$ – effective stress tensor [Pa].

In order to configure the model, while maintaining a high level of reflection of the real system, the following assumptions were made:

- external radiation incident on the module and casing was in the direction normal to the front surface and was considered as direct radiation (no reflected radiation);
- only glass and EVA foil were treated as semi-transparent solid materials;
- thermal boundary conditions for opaque layers were introduced in the form of a constant temperature on the outer surface;
- the radiative heat transfer mechanism was included on all external and internal walls;
- boundary conditions at the inlet were given in the form of a constant temperature equal to the inlet temperature and a uniform velocity, based on the experimental results;
- the boundary condition at the outlet was given in the form of a constant value of atmospheric pressure (101.325 kPa);
- all walls were treated as no-slip;
- the thermophysical properties of the construction materials did not depend on temperature (except for air density);
- potential channel leaks were not taken into account.

The adoption of thermal boundary conditions in the form of a constant temperature on the surface of opaque layers allows the system to be independent of the variability and distribution of temperature in the environment. Experimental measurements have shown that at the same solar irradiance and various air flow rate, the casing temperature differed in the range of 1–2 K. Such difference did not have an impact on the obtained results and could be neglected. Therefore, at a given solar irradiance, the casing temperature can be assumed to be constant.

The calculations used 3D Reynolds-Averaged Navier-Stokes (RANS)

Table 4

Thermophysical properties of the materials used in the CFD model [38,40-42].

Material	Density [kg/m^3]	Specific heat [J/(kg·K)]	Thermal conductivity [W/(m·K)]	Refractive index [-]	Emissivity [-]
Air (25 °C)	1.184	100.43	0.02624	1	–
Wood	700	2310	0.173	–	0.92
Copper	8960	385	398	–	0.65
Glass (3.2 mm)	3000	500	1.8	1.5	0.94
EVA foil (0.5 mm)	960	2090	0.35	1.5	0.94
Silicon cells (0.4 mm)	2330	677	148	–	0.9
PVF (0.1 mm)	1200	1250	0.2	–	0.98

equations and Shear Stress Transport (SST) k-ω turbulence model, suggested in [30,46]. It is a combination of the standard k-ε model with the k-ω model. The k-ε model is used in the fluid core, where turbulent motion occurs. However, the introduction of the k-ω model, allows for better modelling of viscous boundary layers with flow laminarisation and low local Reynolds number values, near to the walls. Due to the wide range of Reynolds numbers, including laminar flow ($Re < 2300$), transitional flow ($2300 < Re < 4000$) and turbulent flow ($Re > 4000$) [33], which results from the change in the hydraulic diameter of the channel, it was decided to use the SST k-ω model, which correctly solves problems at unfavourable pressure gradients and flow separation conditions. The implementation of the SST k-ω model allows avoiding typical issues of standard k-ω models, which are very sensitive to the turbulent properties of the input fluid stream [46]. The Reynolds number was defined as:

$$Re = \frac{\rho \cdot v \cdot D_h}{\mu} \tag{11}$$

where: v – velocity [m/s]; D_h – hydraulic diameter of the air duct [m]; μ – dynamic viscosity [kg/(m•s)].

The hydraulic diameter was defined as:

$$D_h = \frac{4A_f}{P} \tag{12}$$

where: A_f – cross-sectional area of the flow [m^2]; P – wetted perimeter of the cross-section [m];

The turbulence intensity at the inlet was determined by the formula [33]:

$$I_t = 0.16 \cdot Re^{-\frac{1}{8}} \tag{13}$$

The use of the SST k-ω model and the Low Reynolds Number Modelling (LRNM) approach near the wall requires a mesh of high resolution, therefore, the y^+ parameter was controlled:

$$y^+ = \frac{\rho u_T y_p}{\mu} \tag{14}$$

where: u_T – friction velocity at the nearest wall [m/s]; y_p – absolute distance from the wall [m]; μ – dynamic viscosity [kg/(m•s)].

In the case analysed, the meshes used for both heights of the flow duct were characterised by the average values of the y^+ parameter of 1.17 for 25 mm and 1.60 for 50 mm.

The equations of the turbulence kinetic energy and specific dissipation rate for the SST k-ω turbulence model are obtained from a combination of k-ε and k-ω models and given as [46–48]:

$$\frac{D(\rho k)}{Dt} = \nabla \cdot [(\mu + \sigma_k \mu_T) \nabla k] + P_k - \beta^* \rho \omega k \tag{15}$$

$$\frac{D(\rho \omega)}{Dt} = \nabla \cdot [(\mu + \sigma_\omega \mu_T) \nabla \omega] + \gamma \frac{\rho}{\mu_T} P_k - \beta^* \rho \omega^2 + 2(1 - F_1) \rho \sigma_{\omega 2} \frac{\nabla k \cdot \nabla \omega}{\omega} \tag{16}$$

Auxiliary functions, constants, and coefficients of the model are as follows:

$$F_1 = \tanh\left(arg_1^4\right)$$

$$arg_1 = min\left[\max\left(\frac{\sqrt{k}}{\beta^* \omega y_p}, \frac{500\nu}{y_p^2 \omega}\right), \frac{4\rho \sigma_{\omega 2} k}{CD_{k\omega} y_p^2}\right]$$

$$CD_{k\omega} = max\left(\frac{2\rho \sigma_{\omega 2}}{\omega} \nabla \omega \cdot \nabla k, 10^{-10}\right)$$

$$F_2 = \tanh\left(arg_2^2\right)$$

$$arg_2 = \max\left(\frac{2\sqrt{k}}{\beta^* \omega y_p}, \frac{500\nu}{y_p^2 \omega}\right)$$

$$\sigma_k = F_1 \sigma_{k1} + (1 - F_1)\sigma_{k2}$$

$$\sigma_\omega = F_1 \sigma_{\omega 1} + (1 - F_1)\sigma_{\omega 2}$$

$$\beta = F_1 \beta_1 + (1 - F_1)\beta_2$$

$$\gamma = \frac{\beta}{\beta^*} - \frac{\sigma_\omega \kappa^2}{\sqrt{\beta^*}}$$

$$\mu_T = \frac{\rho a_1 k}{max(a_1 \omega, SF_2)} \tag{17}$$

where: k – turbulence kinetic energy [m^2/s^2]; P_k – production term [kg/(m·s^3)]; $\beta^* = 0.09$ [-]; ω – specific dissipation rate [s^{-1}]; $\sigma_{\omega 2} = 0.856$ [-], $\sigma_{k1} = 0.85$ [-]; $\sigma_{k2} = 1.0$ [-]; $\sigma_{\omega 1} = 0.5$ [-]; $\beta_1 = 0.075$ [-]; $\beta_2 = 0.0828$ [-]; $\kappa = 0.41$ [-]; $a_1 = 0.31$ [-]; S – strain rate [s^{-1}]

In order to simulate the radiation incident on the module, the Discrete Ordinates radiation model with the enabled Solar Load module was implemented in a configuration of the grey radiation. This model has some advantages over the alternative ones, the most important of which are the ability to model radiation for semi-transparent materials and the applicability in a wide range of optical depths [39]. It is based on the solution of the radiative transfer equation (RTE), which determines the intensity of radiation I transported from position $\overrightarrow{r}$ towards direction $\overrightarrow{s}$, which is defined as [43,45]:

$$\frac{dI(\overrightarrow{r}, \overrightarrow{s})}{ds} = -(a + \sigma_s)I(\overrightarrow{r}, \overrightarrow{s}) + a\frac{n_{ref}^2 \sigma T^4}{\pi} + \frac{\sigma_s}{4\pi}\int_0^{4\pi} I(\overrightarrow{r}, \overrightarrow{s'})\Phi(\overrightarrow{s} \cdot \overrightarrow{s'})d\Omega' \tag{18}$$

where: I – radiation intensity [W/m^2]; $\overrightarrow{r}$ – position vector [m]; $\overrightarrow{s}$ – unit vector in direction of scattering [-]; s – path length [m]; a – absorption coefficient [1/m]; σ_s – scattering coefficient [1/m]; n_{ref} – refractive index [-]; σ – Stefan-Boltzmann constant [W/(m^2•K^4)]; $\overrightarrow{s'}$ – unit vector in the direction of the incident radiation [-]; Φ – phase function [-]; Ω – solid angle [sr].

In each case, a constant value of solar irradiance was set, equal to the average value obtained from measurements at 9 points. The boundary conditions at the fluid inlet were defined as a constant velocity and temperature of the fluid resulting from the measurements at the experimental stand. The convective heat transfer coefficient defined on the external surface of the module was determined from the formula [46]:

$$h_{nat} = 1.78\left(T_{surf\_avg} - T_{amb\_PV}\right)^{\frac{1}{3}} \tag{19}$$

where: T_{amb_PV} – temperature around the PV roof tile [K].

The calculated value of the heat transfer coefficient, depending on the variant, ranges from 5.02 to 6.95 W/(m^2•K). In the simulations, the average value of 6 W/(m^2•K) was assumed.

The solver has been configured in double precision mode. Coupled pressure-velocity algorithm, least squares cell based spatial discretisation scheme for gradient, second-order spatial discretisation scheme for pressure, and second-order upwind spatial discretisation scheme for other parameters were used to solve the equations.

3. Results and discussion

3.1. Experimental results

The tests were carried out in the range of volumetric air flow rates of
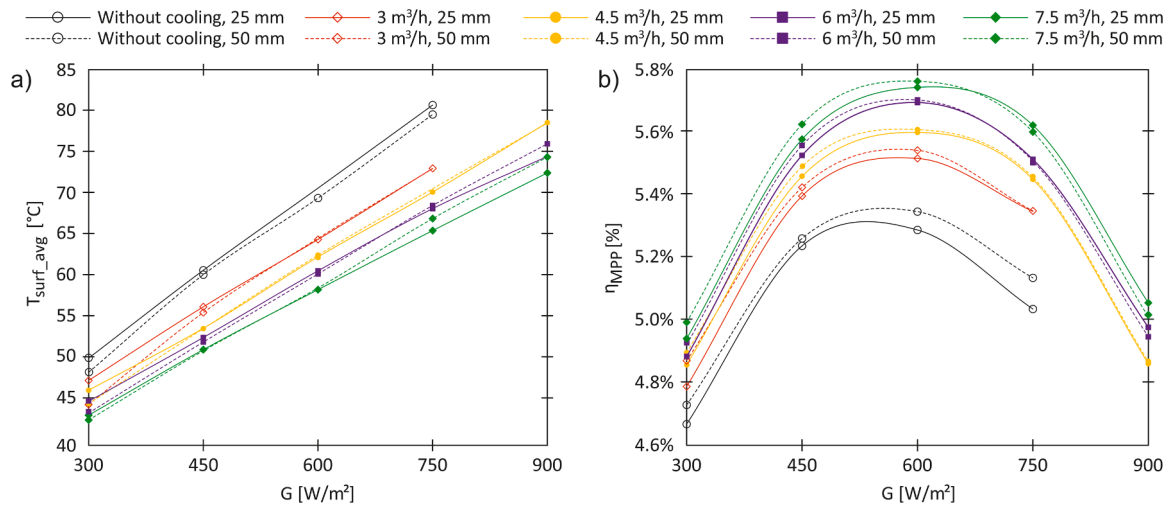
Fig. 6. Experimental results of: (a) temperature profiles of the PV module front surface; (b) electrical efficiency as a function of solar irradiance.

3 to 7.5 m^3/h, in steps of 1.5 m^3/h. As a reference configuration, the system without cooling was tested. Due to the limitations of the PV module permissible operating temperature, variants without cooling and with an air flow of 3 m^3/h, were not considered at the solar irradiance of 900 W/m^2. Fig. 6 presents the average temperature on the front surface and the electrical efficiency of the PV roof tile as a function of the solar irradiance for all analysed configurations.

In the whole range of volume flow rates, at low values of solar irradiance (300–450 W/m^2), lower operating temperature is obtained in the case of a duct with a height of 50 mm. As solar irradiance increases, the average temperature values of the module for both duct heights begin to equalise (at approx. 600 W/m^2). Above 600 W/m^2, the configuration with a lower duct height causes a lower operating temperature. It comes from higher values of velocity of the air flowing through a duct with a lower height. A shorter time of air contact with the hot absorber reduces the temperature of the fluid, and thus improves the conditions for heat removal, lowering the module temperature to a greater extent. At low values of solar irradiance, the absorber temperature is not so high, and the impact of this phenomenon is limited. The influence of the module operating temperature on the generated electrical power is shown in Table 5. In addition, the percentage increase in

the generated power compared to the variants without cooling is shown in the brackets. The results obtained are in line with expectations, according to the theory of the temperature coefficient of the PV module in the MPP.

An important factors for heat recovery are the recovered heat flux and thermal efficiency of the PV roof tile. The family of characteristics of both parameters obtained experimentally, as well as overall efficiency, is presented in Fig. 7.

The results show that in each of the cases analysed, the flow duct with a height of 25 mm allows for more effective heat recovery. The maximum value of the heat flux was 329.8 W/m^2. It was received for a solar irradiance of 900 W/m^2 and an air flow rate of 7.5 m^3/h. Almost linear behaviour of the characteristics is observed for all flow configurations. A slight deviation of the curves in the solar irradiance range from 750 to 900 W/m^2 is noticeable. The coefficients of the linear regression determination R^2 for each curve range from 0.9879 to 0.9983. In the case of thermal efficiency, its decrease is visible with increasing solar irradiance. This is due to the decreasing share of energy that can be received by the cooling air. The temperature difference between the wall and the cooling air in the top parts of the PV roof tile (cells 1, 2, and 3 from Fig. 2) is too small. At the same time, an increasing

Table 5
Electric power generated by the PV roof tile.

| Solar irradiance	Air duct height	Volumetric air flow rate				
		0 m^3/h	3 m^3/h	4.5 m^3/h	6 m^3/h	7.5 m^3/h
		Generated power [W] (Power gain [%])				
300 W/m^2	25 mm	3.09	3.17	3.21	3.23	3.27
		(–)	(2.57 %)	(4.06 %)	(4.61 %)	(5.84 %)
	50 mm	3.13	3.22	3.24	3.26	3.30
		(–)	(2.99 %)	(3.53 %)	(4.08 %)	(5.58 %)
450 W/m^2	25 mm	5.18	5.33	5.39	5.46	5.51
		(–)	(3.03 %)	(4.23 %)	(5.51 %)	(6.49 %)
	50 mm	5.20	5.36	5.43	5.49	5.56
		(–)	(3.09 %)	(4.36 %)	(5.63 %)	(6.91 %)
600 W/m^2	25 mm	6.98	7.28	7.39	7.52	7.58
		(–)	(4.31 %)	(5.88 %)	(7.68 %)	(8.60 %)
	50 mm	7.06	7.32	7.41	7.53	7.61
		(–)	(3.65 %)	(4.89 %)	(6.65 %)	(7.77 %)
750 W/m^2	25 mm	8.32	8.83	9.00	9.10	9.28
		(–)	(6.18 %)	(8.21 %)	(9.47 %)	(11.63 %)
	50 mm	8.48	8.83	9.01	9.09	9.25
		(–)	(4.16 %)	(6.24 %)	(7.25 %)	(9.06 %)
900 W/m^2	25 mm			9.63	9.86	10.01
				(–)	(–)	(–)
	50 mm			9.64	9.80	9.92
				(–)	(–)	(–)
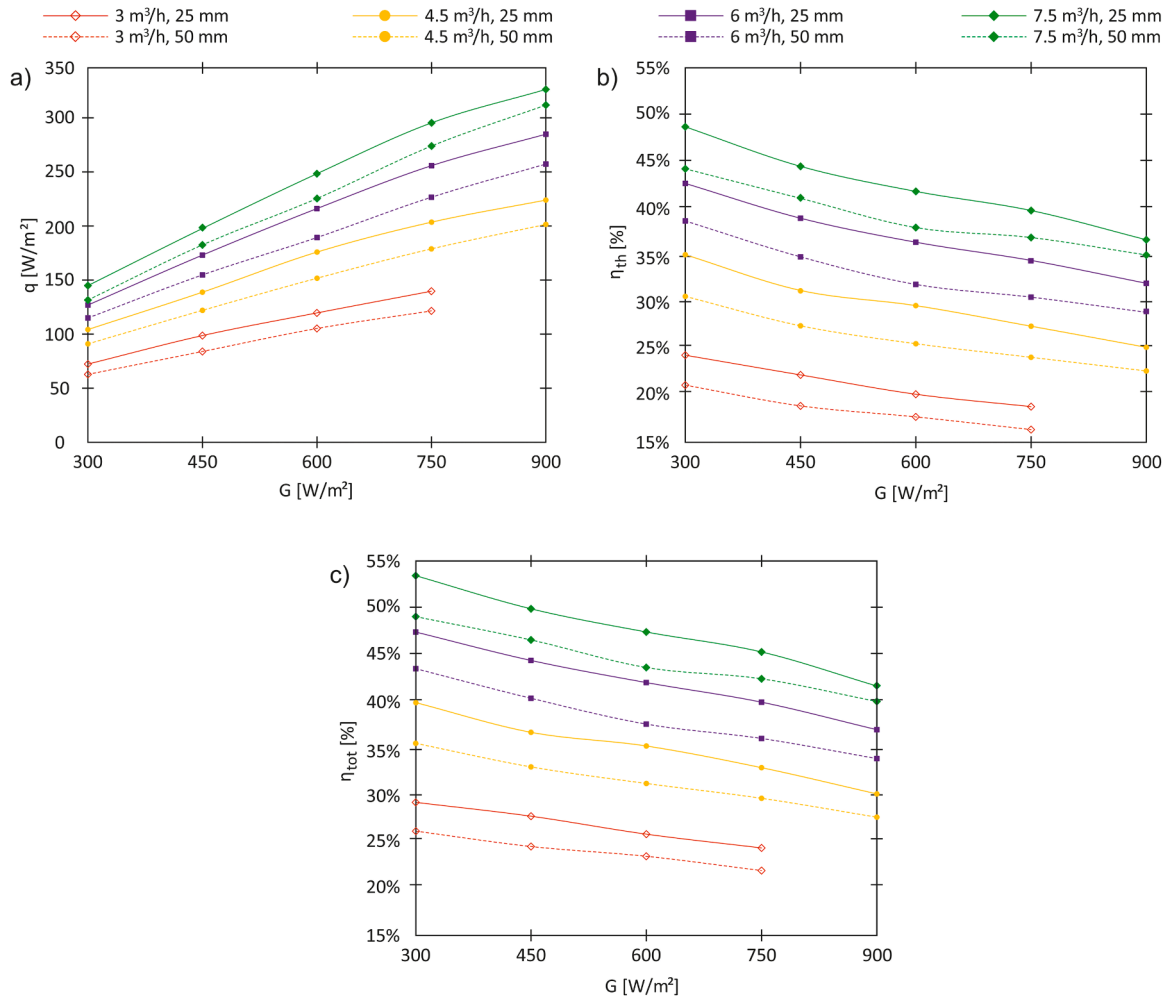
Fig. 7. Experimental characteristics of: (a) heat flux received by cooling air; (b) thermal efficiency; (c) overall efficiency of PV roof tile as a function of solar irradiance.

part of the heat is dissipated to the environment and does not contribute to the useful heat of the analysed thermodynamic system. The total efficiency strongly depends on the thermal efficiency value, which is many times higher than the electrical efficiency obtained at each measurement point. This implies a similar shape of the characteristics obtained for both parameters. The highest total efficiency value of 53.64 % was obtained for a channel with a height of 25 mm, with solar irradiance of 300 W/m^2 and a volumetric air flow rate of 7.5 m^3/h. The lowest heat loss to the environment corresponding to this case was 46.36 % of the total energy supplied to the system.

3.2. Uncertainty analysis

With regard to the experimental studies, an analysis of the measurement uncertainties was performed. The number of measurements carried out in each series did not allow for the statistical approach to the uncertainties. The focus was therefore on the systematic analysis of er-

rors. The parameters presented in the characteristics that describe the operation of the system under given conditions are the result values that have not been measured directly. For this reason, the analysis was based on the principle of uncertainty propagation, which is described by the formula [49]:

$$\Delta y = \sqrt{\sum_{j=1}^{m}\left(\left|\frac{\partial y}{\partial x_j}\right|\Delta(x_j)\right)^2} \tag{20}$$

where: y – function describing a given quantity; x_j – measured variable; $\Delta(x_j)$ – measurement uncertainty of a device measuring the value of a variable x_j; j – variable number; m – number of variables in the function

Based on the data listed in Table 3 the absolute uncertainties of the quantities presented were calculated and summarised in Table 6.

3.3. CFD results

As in the case of experimental studies, the characteristics obtained numerically were plotted as a function of the solar irradiance. Fig. 8 shows the obtained front surface temperature profiles, received heat flux and thermal efficiency of the PV roof tile. At this stage, the CFD simulations focused only on the aspect of thermal efficiency, so the electrical and general efficiency characteristics were not taken into account.

The characteristics are similar to those obtained from the experiment. To assess the quality of the numerical model and the degree of the mapping of experimental data, a relative difference in the values of
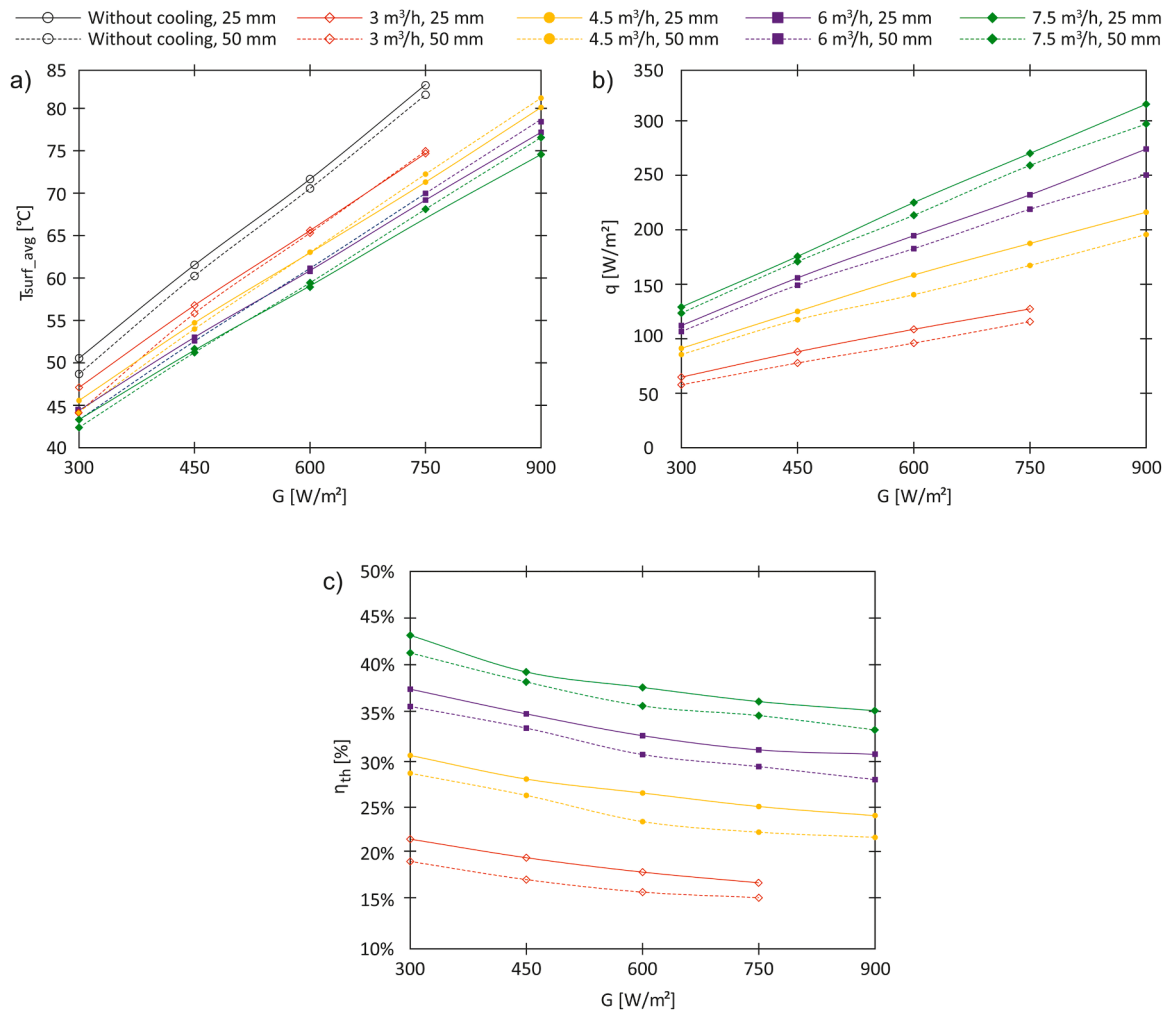
Table 6
Summary of the uncertainty analysis.

Parameter	Absolute uncertainty
Average temperature on the front surface of the module	0.5 K
Electrical power	0.61–0.77 W
Electrical efficiency	0.39–1.34 %
Heat flux	0.21–4.99 W/m^2
Thermal efficiency	0.07–6.51 %

Fig. 8. Numerical characteristics of: (a) temperature on the front surface; (b) heat flux received by the cooling air; (c) thermal efficiency of the PV roof tile.

Table 7
Relative differences between numerical and experimental results.

Solar irradiance	Height of the air flow duct	Difference of average front surface temperature	Difference of outlet temperature	Difference of the heat flux	Difference of thermal efficiency
300 W/m²	25 mm	0.04 %	−0.68 %	−11.37 %	−4.30 %
	50 mm	0.04 %	−0.36 %	−6.83 %	−2.25 %
450 W/m²	25 mm	0.30 %	−0.84 %	−10.45 %	−3.58 %
	50 mm	0.19 %	−0.38 %	−5.29 %	−1.58 %
600 W/m²	25 mm	0.34 %	−0.97 %	−9.63 %	−3.09 %
	50 mm	0.36 %	−0.56 %	−6.27 %	−1.65 %
750 W/m²	25 mm	0.56 %	−1.02 %	−8.64 %	−2.60 %
	50 mm	0.61 %	−0.53 %	−5.02 %	−1.35 %
900 W/m²	25 mm	0.74 %	−0.46 %	−3.58 %	−1.12 %
	50 mm	0.86 %	−0.40 %	−3.46 %	−1.04 %

selected parameters was determined for each case analysed. They were calculated according to the following formula:

$$\delta = \frac{x_{CFD} - x_{ex}}{x_{ex}} \quad (21)$$

where: x_{CFD} – value of the parameter obtained from CFD calculations; x_{ex} – value of the parameter obtained from the experiment.

Table 7 shows the averaged relative differences between the results obtained for each series with different solar irradiance values, averaged for the volumetric air flow rates analysed.

For a transparency of the presentation, in the case of thermal effi-

ciency, the absolute difference was considered:

$$\Delta\eta_{th} = \left(\eta_{th_{CFD}} - \eta_{th_{ex}}\right) \quad (22)$$

where: $\eta_{th_{CFD}}$ – value of the thermal efficiency determined on the basis of the CFD calculations [-]; $\eta_{th_{ex}}$ – value of the thermal efficiency determined in the basis of the experimental data [-].

The maximum difference in the average absolute temperature of the front surface of the module is 0.86 %. The value of the heat flux deviates by a maximum of −11.37 %, which translates into a difference in thermal efficiency of −4.30 %. Slight overestimation of the average
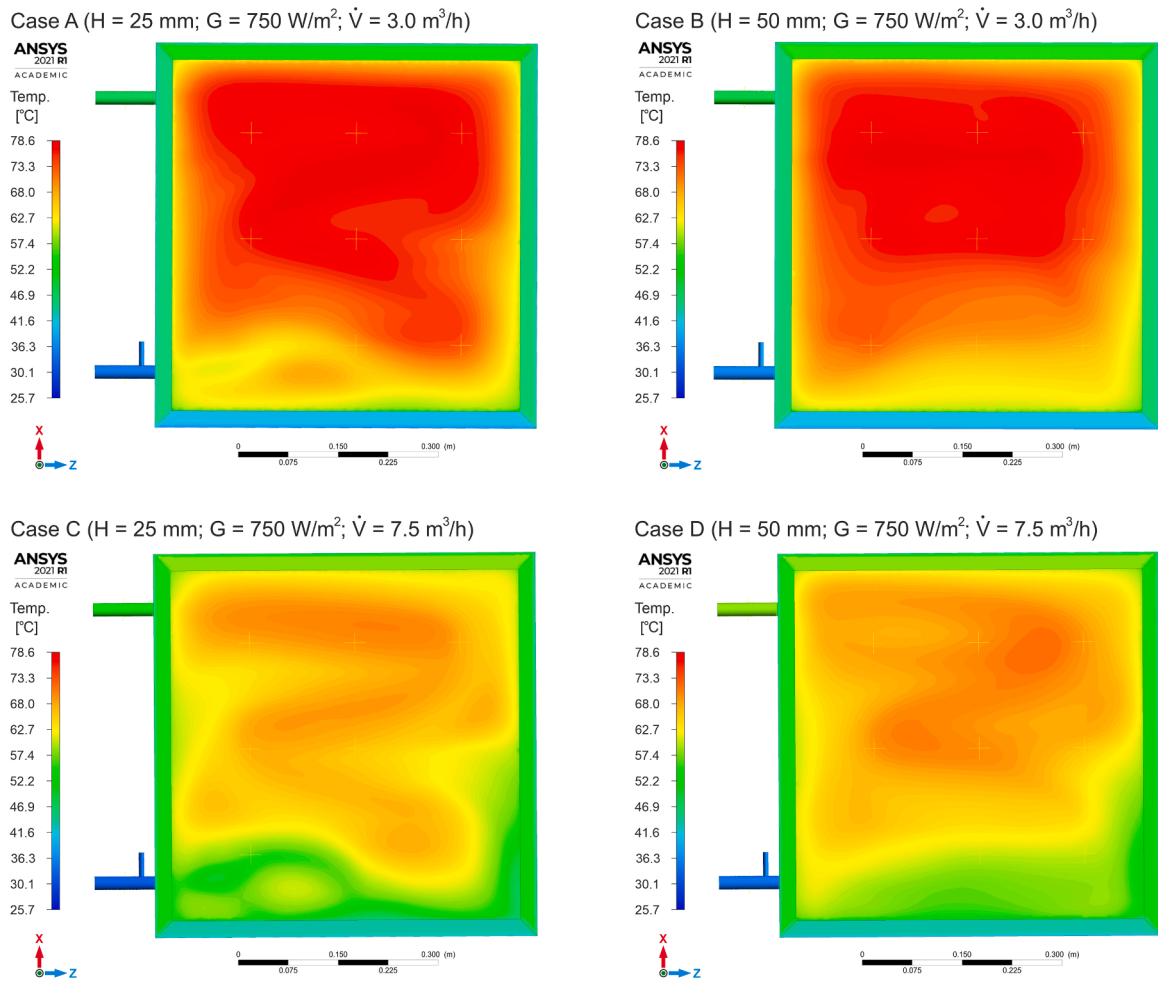
Fig. 9. Temperature distribution on the front surface for variants with a solar irradiance of 750 W/m^2 for Cases A, B, C and D.
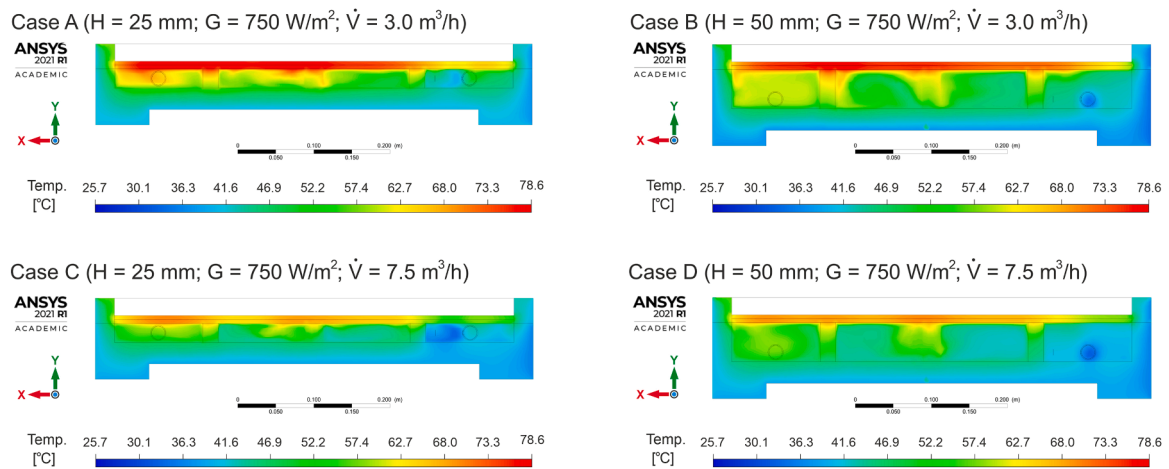

Fig. 10. Temperature distribution in the cross-section (xy) located in the middle of the first row of silicon cells (Nos. 1, 4, 7 from Fig. 2), the solar irradiance equal to 750 W/m^2, for Cases A, B, C and D.

front surface temperature was found. Small differences in the values obtained are also visible in the case of the heat flux and thermal efficiency. The differences are mainly attributed to factors such as: the use of halogen light simulator with a slightly different emission spectrum than sunlight; the use of a radiation model considering only grey radiation; the nonuniformity of the distribution of solar irradiance on the surface of the PV roof tile; utilisation of boundary conditions for the

casing in the form of a homogeneous temperature, equal to the temperature at the geometric centre of each wall; the use of an averaged value of the convective heat transfer coefficient for the face of the PV module, the impossibility of obtaining an ideal steady state, measurement uncertainties of the considered quantities, potential differences in the thermophysical properties of the materials used, deviations in the position of the temperature measurement point at the outlet of the air
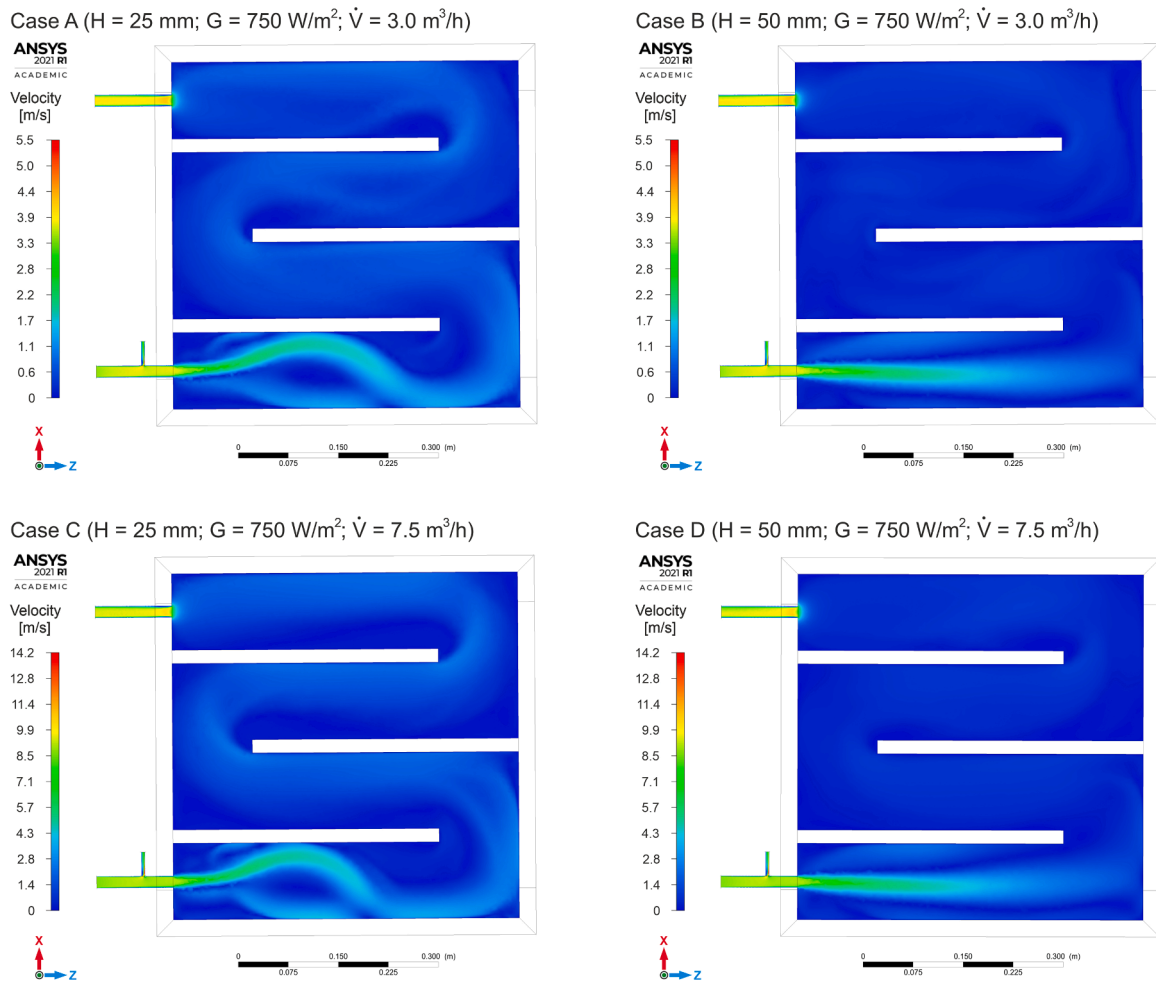
12

Fig. 11. Velocity distribution in the longitudinal cross-section (*xz*) for Cases A, B, C and D.

flow channel relative to the pipe axis. However, the similarity of the results obtained for both research paths can be considered high. The consistency of the results confirms the readiness of the proposed CFD model for further parametric analysis and system optimisation.

In Figs. 9–12 the numerical results are presented for selected cases named Case A, Case B, Case C and Case D. All cases represent conditions of the solar irradiance of 750 W/m². Cases A and C show the results for the duct height equal to 25 mm and the air flow rate 3 m³/h and 7.5 m³/h, respectively, while Cases B and D show the results for the duct height equal to 50 mm and the air flow rate 3 m³/h and 7.5 m³/h, respectively.

Fig. 9 shows the front surface temperature distribution for selected cases. The points where the temperature was controlled were marked with a yellow plus sign. Fig. 10 presents the temperature distribution in the cross-section (*xy*) of the whole system, located in the middle of the first vertical row of silicone cells (No. 1, 4 and 7 described in Fig. 2). For both figures, a uniform colour scale is used to facilitate the capture of differences between individual configurations.

Fig. 11 indicates a velocity distribution presented in the longitudinal cross-section (*xz*), located at the height of the middle of inlet pipe, while Fig. 12 shows the streamlines obtained for the air flow, from the top view. For the same air flow rate values, to better visualise the phenomena and make it easier to compare the results, the same scale was used in both variants of the channel height.

In the case of both analysed values of volumetric air flow rate, the greatest differences in temperature distributions on the front surface of the module between the 25 and 50 mm high channels occur in the area of cells Nos. 7–9, located in the lower part of the module. This area is characterised by a different distribution of velocity and streamlines. In

the channel with a smaller height, the main stream of the air flowing out of the inlet deflects towards the partition, in the area of cell No. 7. Part of the air flow also deflects towards the lower wall of the casing. In Fig. 9, the zone of lower temperature in the area of the main flow stream is clearly visible. At the level of cells Nos. 7 and 8, vortices are formed and concentrated under the middle and lower parts of the cells. Then, in the area of cell No. 8, the main flow stream deflects towards the lower wall of the casing, and then changes the direction forced by the partition.

In the case of a channel with a height of 50 mm, the main flow stream, after leaving the inlet pipe, follows the *z* axis towards the side wall, deflecting upwards forced by the structure of the flow channel. In the top part of the zone located under cells Nos. 7 and 8, a vortex with a low flow velocity is created. In a channels of both height values, in the zone of changing the flow direction at the first partition, in the *xz* cross-section, the flow mixes. Better mixing in the *xz* direction is observed for the 50 mm channel, which is confirmed by the obtained air velocity distribution and the plotted streamlines. As a result, the temperature distribution on the front surface is slightly more uniform in this case. Areas of stagnation are visible in the case of both flow channels in a vicinity of the left casing wall at the level of the second partition and the right casing wall at the level of the third partition. The air with the highest temperature is in the zone located under cell No. 1, closest to the outlet (Fig. 10). This is due to the longer residence time of the air in the flow channel. At the same time, in each zone between the partitions or partitions and the side walls of the casing, the air with the highest temperature is close to the absorber. The obtained temperature distribution indicates insufficient air mixing in the *y* direction, characteristic for both flow channels. Slightly better mixing is visible in the channel
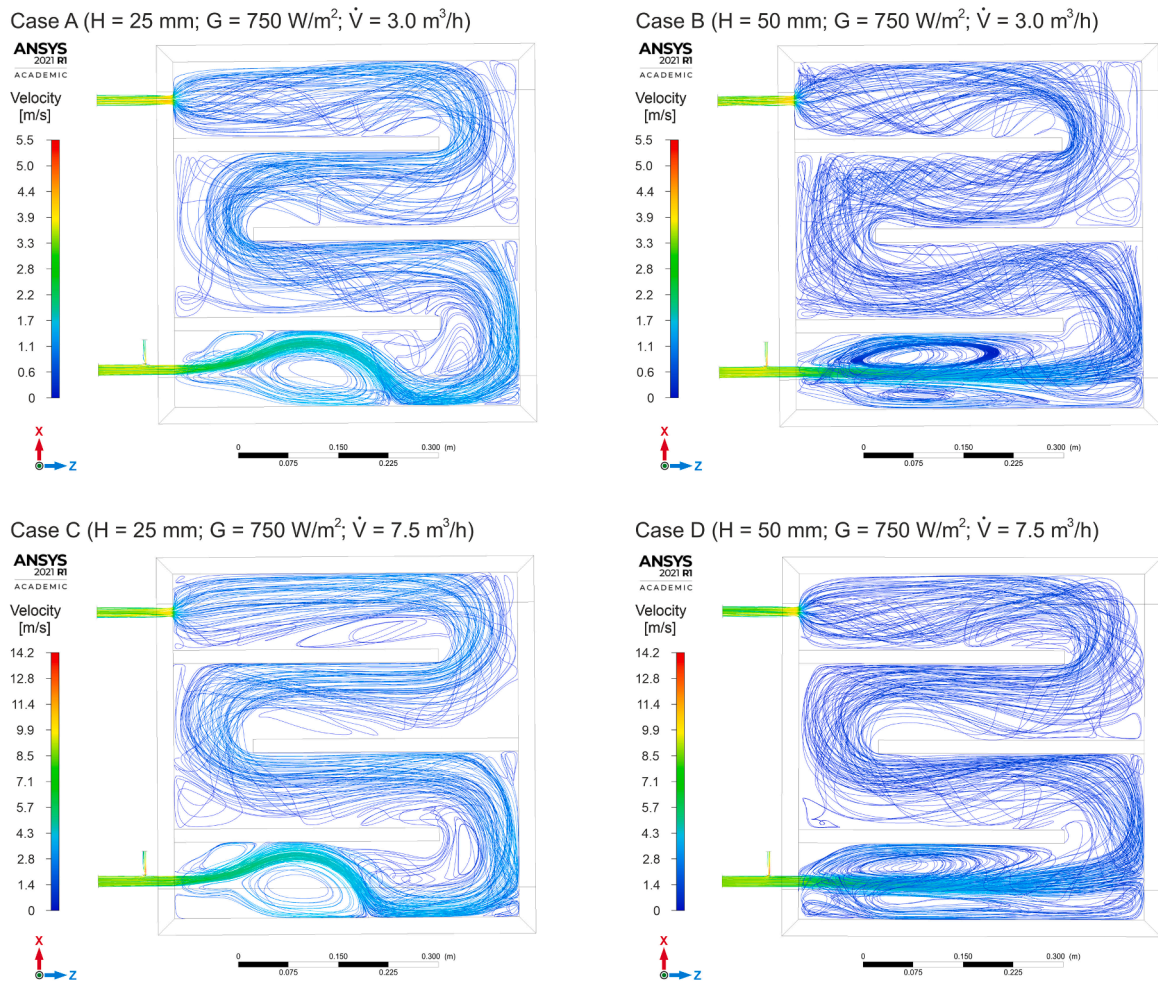
Fig. 12. Streamlines presented from the top view for Cases A, B, C, and D.

Table 8
Comparison of own performance indicators and those published.

No.	Reference / Year	Type of study		Mass flow rate [kg/s]	Electrical efficiency increase [%]	Thermal efficiency [%]
		Exp.	Num.			
1	Authors' results	+	+	0.001–0.0025	2.57–11.63	21.7–53.64
2	[32] / 2023	+	–	0.04–0.08	11–12.6	–
3	[30] / 2023	+	+	0.374	–	8.2–10.7
4	[28] / 2019	+	–	0.0047–0.0165	–	20–31
5	[50] / 2017	–	+	0.023	0.66	21.19
6	[51] / 2017	+	–	0.011–0.037	11.6	2–48

with a smaller height, which improves heat removal. This exhibits demand for methods to intensify heat exchange leading to better mixing of air in the flow channel, which may significantly improve the removal of heat and reduction of the operating temperature of PV cells.

3.4. Verification and discussion of results

In order to verify the results, the obtained electrical and thermal efficiency were compared with the values reported in the literature. Reference was made to works dedicated to air cooling of PV/T and BIPV/T collectors with channels placed under the absorber. The verification results are presented in Table 8. In the case of electrical efficiency, the net relative increase compared to the reference variant without cooling was highlighted.

Direct comparison of results obtained in various studies is not possible. This is due to many factors, such as the method of conducting research, different types and dimensions of modules used, different measuring equipment, different values of ambient temperature, solar irradiance tested, wind speeds and their large variability, as well as different boundary conditions, assumptions and models adopted in numerical simulations. However, considering the own results in relation to the results reported in the literature and briefly summarised in Table 8, following observations and conclusions can be formulated:

- The flow rate values applied in this article (approximately 0.001–0.0025 kg/s) were lower than those used by other researchers. This is due to the dimensions and structure of the tested PV roof tile, as well as the willingness to assess the behaviour of the system at low flow rates.
- The obtained electrical efficiency values are similar to those reported in the literature. They are a consequence of taking into account all variants that cover a wide range of input variables.

14

- The thermal efficiency values are consistent with the reports in the literature, reaching high values for selected configurations of input variables. This is due to the use of partitions that direct the flow of the medium in the flow channel. The contact time of the air with the hot absorber is longer, which translates into a greater amount of heat removed by the air than in the case of single-pass flow.
- For a channel with a smaller height, higher thermal efficiency values were obtained in each analysed configuration. The influence of the channel height on the electrical efficiency of the module is small. Similar results and conclusions have been reported in publications [31,33].
- According to previous studies presented in the literature [28,31-33], increasing the air flow rate reduces the module operating temperature and improves its electrical, thermal and overall efficiency. The increase in thermal efficiency occurs to a much greater extent than the increase in electrical efficiency.
- Similarly to the work [14,30], the results obtained based on CFD analyses and experimental tests were highly consistent. In the case of the average temperature on the front surface of the module, the absolute differences obtained by the mentioned researchers were approximately 2 K and 2.07 K, respectively. In the presented work, taking into account all the configurations considered, these differences range from 0.07 to 3.20 K.

4. Conclusions

The article presents the results of research on the influence of air cooling conditions of a photovoltaic roof tile and the height of the flow channel (25 and 50 mm) on its electrical and thermal efficiency. The motivation to carry out work in this area was a pertinence of forced cooling of BIPV/T modules, which are particularly exposed to operation at elevated temperatures. A literature gap was found among works dedicated to this type of system, which would comprehensively address the issues of the influence of the height of the flow channel and other input variables on the obtained results. Continuing the work carried out by the authors, the focus was on the development of a dedicated numerical model and its verification using an experimental stand.

The results obtained by both approaches confirmed a significant impact of the considered input variables on the obtained performance indicators. It was found that the height of the flow channel has a great influence on the possibility of heat recovery, but a small one on the achieved electrical efficiency. The maximum increase in electrical power recorded as a result of the use of cooling was 11.63 %. It was obtained for an air duct height of 25 mm, at a solar irradiance of 750 W/m^2 and an air flow rate of 7.5 m^3/h. The system with the highest thermal potential turned out to be the configuration with a channel height of 25 mm. The highest heat flux was 329.84 W/m^2 and was obtained at a solar irradiance of 900 W/m^2 and a volumetric flow rate of 7.5 m^3/h. Under the same cooling conditions, but with a solar irradiance of 300 W/m^2, the highest thermal efficiency value was obtained equal to 48.70 %. It has been proven that a higher flow rates increases the removed heat flux and improves the thermal efficiency.

A high correspondence between the experimental results and the CFD simulation results was highlighted. The average relative differences between the parameters considered were at the level of several percent. Thus, the usefulness of the model for further research was demonstrated. Differences in the cooling air flow conditions and temperature distributions obtained for both flow channel heights were visualised, providing information on the mechanisms behind them. Differences in a flow structure have consequences in a form of higher thermal efficiency values and increased heat recovery potential for a configuration with a lower channel height. The authors hope that the presented research contributes to filling the literature gap and helps to understand the phenomena occurring in photovoltaic/thermal systems. This knowledge will enable the effective use of CFD tools in planned research on methods to intensify heat transfer from air-cooled photovoltaic roof tiles.

CRediT authorship contribution statement

Jakub Lukasik: Conceptualization, Data curation, Formal analysis, Investigation, Methodology, Software, Validation, Visualization, Writing – original draft, Writing – review & editing. **Jan Wajs:** Writing – original draft, Validation, Supervision, Project administration, Methodology, Investigation, Funding acquisition, Formal analysis, Writing – review & editing, Conceptualization.

Declaration of competing interest

The authors declare that they have no known competing financial interests or personal relationships that could have appeared to influence the work reported in this paper.

Data availability

Data will be made available on request.

Acknowledgements

References

[1] Renewable energy statistics 2023, IRENA Report, 2023.
[2] J. Aizarani, Primary energy consumption worldwide from 2000 to 2021, Statista (2023).
[3] M. Herrando, K. Wang, G. Huang, T. Otanicar, O.B. Mousa, R.A. Agathokleous, Y. Ding, S. Kalogirou, Ekins-Daukes Ned, R.A. Taylor, C.N. Markides, A review of solar hybrid photovoltaic-thermal (PV-T) collectors and systems, Prog. Energy Combust. Sci. 97 (2023) 101072, https://doi.org/10.1016/j.pecs.2023.101072.
[4] J. Čurpek, M. Čekon, O. Šikula, R. Slávik, Thermodynamic responses of adaptive mechanisms in BiPV façade systems coupled with latent thermal energy storage, Energy Build. 279 (2023) 112665, https://doi.org/10.1016/j.enbuild.2022.112665.
[5] S. Margoum, C. El Fouas, H. Bekkay, S. Aneli, A. Gagliano, G. Mannino, G.M. Tina, Study effect of nanofluids on the performance enhancement of PV/T collector, in: Proceedings of the 3rd International Conference on Electronic Engineering and Renewable Energy Systems. ICEERE 2022. Lecture Notes in Electrical Engineering 954, 2023, https://doi.org/10.1007/978-981-19-6223-3_93. Springer.
[6] J. Shi, Z. Quan, L. Wang, Y. Wang, H. Ren, Y. Zhao, Performance of a BAPVT modules coupled TEHR unit fresh air system based on micro heat pipe array, Part C, Appl. Thermal Eng. 236 (2024) 121690, https://doi.org/10.1016/j.applthermaleng.2023.121690.
[7] B. Du, Z. Quan, L. Hou, Y. Zhao, X. Lou, S. Shao, Simulation analysis of a photovoltaic/thermal-air dual heat source direct-expansion heat pump, Renew. Energy 218 (2023) 119019, https://doi.org/10.1016/j.renene.2023.119019.
[8] H. Gürbüz, S. Demirtürk, H. Akçay, Ü. Topalcı, Thermal stabilization and energy harvesting in a solar PV/T-PCM-TEG hybrid system: a case study on the design of system components, Energy Convers. Manage 294 (2023) 117536, https://doi.org/10.1016/j.enconman.2023.117536.
[9] A.M.A. Alshibil, I. Farkas, P. Víg, Experimental performance comparison of a novel design of bi-fluid photovoltaic-thermal module using Louver fins, Energy Reports 9 (2023) 4518–4531, https://doi.org/10.1016/j.egyr.2023.03.110.
[10] H. Perez, J.G. Carrillo, A. Bassam, B. Flota-Banuelos, L.D. Patino-Lopez, Thermal performance of a discontinuous finned heatsink profile for PV passive cooling, Appl. Therm. Eng. 184 (2021) 116238, https://doi.org/10.1016/j.applthermaleng.2020.116238.
[11] K. Anusuya, K. Vijayakumar, S. Manikandan, From efficiency to eternity: a holistic review of photovoltaic panel degradation and End-of-Life management, Solar Energy 265 (2023) 112135, https://doi.org/10.1016/j.solener.2023.112135.
[12] E.D. Rounis, A. Athienitis, T. Stathopoulos, Review of air-based PV/T and BIPV/T systems - Performance and modelling, Renew. Energy 163 (2021) 1729–1753, https://doi.org/10.1016/j.renene.2020.10.085.
[13] G. Aspetakis, Q. Wang, Critical review of Air-Based PVT technology and its integration to building energy systems, Energy Built Environ. (2023) https://doi.org/10.1016/j.enbenv.2023.10.001 (in press).
[14] E. Arslan, M. Aktaş, Ö.F. Can, Experimental and numerical investigation of a novel photovoltaic thermal (PV/T) collector with the energy and exergy analysis, J. Clean. Prod. 276 (2020) 123255, https://doi.org/10.1016/j.jclepro.2020.123255.
[15] E.Y. Gürbüz, B. Kusun, A.D. Tuncer, T. Ural, Experimental investigation of a double-flow photovoltaic/thermal air collector with natural dolomite powder-

embedded thermal energy storage unit, J. Energy Storage 64 (2023) 107220, https://doi.org/10.1016/j.est.2023.107220.

[16] M. Al-Damook, Z. Khatir, M.A. Qubeissi, D. Dixon-Hardy, P.J. Heggs, Energy efficient double-pass photovoltaic/thermal air systems using a computational fluid dynamics multi-objective optimisation framework, Appl. Therm. Eng. 194 (2021) 117010, https://doi.org/10.1016/j.applthermaleng.2021.117010.

[17] E.D. Rounis, A.K. Athienitis, T. Stathopoulos, Multiple-inlet Building Integrated Photovoltaic/Thermal system modelling under varying wind and temperature conditions, Solar Energy 139 (2016) 157–170, https://doi.org/10.1016/j.solener.2016.09.023.

[18] D. Jin, S. Quan, J. Zuo, S. Xu, Numerical investigation of heat transfer enhancement in a solar air heater roughened by multiple V-shaped ribs, Renew. Energy 134 (2019) 78–88, https://doi.org/10.1016/j.renene.2018.11.016.

[19] P. Promvonge, P. Promthaisong, S. Skullong, Experimental and numerical thermal performance in solar receiver heat exchanger with trapezoidal louvered winglet and wavy groove, Solar Energy 236 (2022) 153–174, https://doi.org/10.1016/j.solener.2022.02.052.

[20] A.S. Yadav, M.K. Dwivedi, A. Sharma, V.K. Chouksey, CFD based heat transfer correlation for ribbed solar air heater, Proceedings 62 (Part 3) (2022) 1402–1407, https://doi.org/10.1016/j.matpr.2021.12.382.

[21] A.S. Yadav, O.P. Shukla, A. Sharma, I.A. Khan, CFD analysis of heat transfer performance of ribbed solar air heater, Proceedings 62 (Part 3) (2022) 1413–1419, https://doi.org/10.1016/j.matpr.2021.12.560.

[22] S. Zahran, A.A. Sultan, M. Bekheit, M.R. Elmarghany, Heat transfer augmentation through rectangular cross section duct with one corrugated surface: an experimental and numerical study, Case Stud. Thermal Eng. 36 (2022) 102252, https://doi.org/10.1016/j.csite.2022.102252.

[23] A.N. Özakin, F. Kaya, Effect on the exergy of the PVT system of fins added to an air-cooled channel: a study on temperature and air velocity with ANSYS Fluent, Solar Energy 184 (2019) 561–569, https://doi.org/10.1016/j.solener.2019.03.100.

[24] A.M. Elbreki, A.F. Muftah, K. Sopian, H. Jarimi, A. Fazlizan, A. Ibrahim, Experimental and economic analysis of passive cooling PV module using fins and planar reflector, Case Stud. Thermal Eng. 23 (2021) 100801, https://doi.org/10.1016/j.csite.2020.100801.

[25] T. Hai, I.B. Mansir, A. Alshuraiaan, A.M. Abed, H. Elhosiny Ali, M. Dahari, H. Albalawi, Numerical investigation on the performance of a solar air heater using inclined impinging jets on absorber plate with parallel and crossing orientation of nozzles, Case Stud. Thermal Eng. 45 (2023) 102913, https://doi.org/10.1016/j.csite.2023.102913.

[26] C. Yüksel, M. Öztürk, E. Çiftçi, Analysis of a novel V-grooved double pass photovoltaic thermal solar dryer including thermal energy storage, Applied Thermal Engineering, Part C 236 (2024) 121697, https://doi.org/10.1016/j.applthermaleng.2023.121697.

[27] H.A. Kazem, A.H.A. Al-Waeli, M.T. Chaichan, K. Sopian, A.S. Al Busaidi, A. Gholami, Photovoltaic-thermal systems applications as dryer for agriculture sector: a review, Case Studies in Thermal Engineering 47 (2023) 103047, https://doi.org/10.1016/j.csite.2023.103047.

[28] P. Jha, B. Das, R. Gupta, An experimental study of a photovoltaic thermal air collector (PVTAC): a comparison of a flat and the wavy collector, Appl. Therm. Eng. 163 (2019) 114344, https://doi.org/10.1016/j.applthermaleng.2019.114344.

[29] Y. Xie, J. Zhou, E. Bisengimana, F. Jiang, W. Ji, L. Sun, K. Zhao, Y. Yuan, Exergy performance assessment of a novel air-cooled photovoltaic thermal collector with a double serpentine runner, Appl. Therm. Eng. 236 (Part A) (2024) 121330, https://doi.org/10.1016/j.applthermaleng.2023.121330.

[30] A. Hussien, A. Eltayesh, H.M. El-Batsh, Experimental and numerical investigation for PV cooling by forced convection, Alexandria Eng. J. 64 (2023) 427–440, https://doi.org/10.1016/j.aej.2022.09.006.

[31] A. Kasaeian, Y. Khanjari, S. Golzari, O. Mahian, S. Wongwises, Effects of forced convection on the performance of a photovoltaic thermal system: an experimental study, Exp. Therm. Fluid. Sci. 85 (2017) 13–21, https://doi.org/10.1016/j.expthermflusci.2017.02.012.

[32] M. Patil, A. Sidramappa, S.K. Shetty, A.M. Hebbale, Experimental study of solar PV/T panel to increase the energy conversion efficiency by air cooling, Proceedings 92 (Part 1) (2023) 309–313, https://doi.org/10.1016/j.matpr.2023.05.007.

[33] N.A. Dunne, P. Liu, A.F.A. Elbarghthi, Y. Yang, V. Dvorak, C. Wen, Performance evaluation of a solar photovoltaic-thermal (PV/T) air collector system, Energy Convers. Manage. 20 (2023) 100466, https://doi.org/10.1016/j.ecmx.2023.100466.

[34] P. Mauszczyk, T. Popławski, J. Flasza, The influence of solar irradiance and module temperature on selected parameters and rated power of the photovoltaic panels (in Polish), Przegląd Elektrotechniczny 91 (2015) 159–162, https://doi.org/10.15199/48.2015.12.40.

[35] J. Wajs, A. Golabek, R. Bochniak, D. Mikielewicz, Air-cooled photovoltaic roof tile as an example of the BIPVT system – An experimental study on the energy and exergy performance, Energy 197 (2020) 117255, https://doi.org/10.1016/j.energy.2020.117255.

[36] J. Wajs, A. Golabek, R. Bochniak, Photovoltaic roof tiles: the influence of heat recovery on overall performance, Energies. (Basel) 12 (2019) 4097, https://doi.org/10.3390/en12214097.

[37] C. Şirin, J. Goggins, M. Hajdukiewicz, A review on building-integrated photovoltaic/thermal systems for green buildings, Appl. Therm. Eng. 229 (2023) 120607, https://doi.org/10.1016/j.applthermaleng.2023.120607.

[38] W.Z. Leow, Y.M. Irwan, I. Safwati, M. Irwanto, A.R. Amelia, Z. Syafiqah, M.I. Fahmi, N. Rosle, Simulation study on photovoltaic panel temperature under different solar radiation using computational fluid dynamic method, J. Phys. 1432 (2020) 012052, https://doi.org/10.1088/1742-6596/1432/1/012052.

[39] S.R. Maadi, M. Khatibi, E. Ebrahimnia-Bajestan, D. Wood, Coupled thermal-optical numerical modeling of PV/T module – Combining CFD approach and two-band radiation DO model, Energy Convers. Manage 198 (2019) 111781, https://doi.org/10.1016/j.enconman.2019.111781.

[40] Engineering ToolBox (2001). https://www.engineeringtoolbox.com [accessed on 06.04.2023].

[41] A. Shamim, M. Noman, M. Zubair, A.D. Khan, S. Saher, A facile approach to determine the unknown refractive index (n) and extinction coefficient (k) of novel encapsulant materials used in back contact PV modules, Appl. Phys. A 124 (2018) 542, https://doi.org/10.1007/s00339-018-1974-x.

[42] I. Guarracino, A. Mellor, N.J. Ekins-Daukes, C. Markides, Dynamic coupled thermal-and-electrical modelling of sheet-and-tube hybrid photovoltaic/thermal (PVT) collectors, Appl. Therm. Eng. 101 (2016) 778–795, https://doi.org/10.1016/j.applthermaleng.2016.02.056.

[43] Ansys Fluent Theory Guide 15, Canonsburg, PA, 2013, pp. 2-3, 133–134.

[44] D. Tomkiewicz, A. Cudzewicz, J. Gorecka-Orzechowska, Application of the Fluent program for modeling thermodynamic phenomena in a climatic chamber (in Polish), Agricult. Eng. (in Polish) 6 (2011) 239–245.

[45] M. Pawlucki, M. Krys, CFDs for engineers. practical exercises on the example of the ansys fluent system (in Polish), Gliwice, Helion SA, 2020, pp. 249–256.

[46] S. Sandooghdar, S. Akbarzadeh, M.S. Valipour, A. Arabkoohsar, Performance improvement of air-based solar photovoltaic/thermal collectors using wavy channels, Renew. Energy 211 (2023) 831–845, https://doi.org/10.1016/j.renene.2023.05.043.

[47] A.A. Matyushenko, A.V. Garbaruk, Adjustment of the k-ω SST turbulence model for prediction of airfoil characteristics near stall, J. Phys. 769 (2016) 012082, https://doi.org/10.1088/1742-6596/769/1/012082.

[48] K. Hanjalic, Closure models for incompressible turbulent flows, in: C. Benocci, J.P. A.J. van Beeck (Eds.), Von Karman Lecture Series 2004/2005, Von Karman Institutes Fluid Dynamics, 2004, pp. 1–75.

[49] R.J. Moffat, Describing the uncertainties in experimental results, Exp. Therm. Fluid. Sci. 1 (1988) 3–17, https://doi.org/10.1016/0894-1777(88)90043-X.

[50] M.E.A. Slimani, M. Amirat, I. Kurucz, S. Bahria, A. Hamidat, W.B. Chaouch, A detailed thermal-electrical model of three photovoltaic/thermal (PV/T) hybrid air collectors and photovoltaic (PV) module: comparative study under Algiers climatic conditions, Energy Convers. Manage 133 (2017) 458–476, https://doi.org/10.1016/j.enconman.2016.10.066.

[51] H. Saygin, R. Nowzari, N. Mirzaei, L.B.Y. Aldabbagh, Performance evaluation of a modified PV/T solar collector: a case study in design and analysis of experiment, Solar Energy 141 (2017) 210–221, https://doi.org/10.1016/j.solener.2016.11.048.